



Effects of local gas diffusion layer gas permeability variations on spatial proton exchange membrane fuel cells performance

Tatyana V. Reshetenko*, Jean St-Pierre, Richard Rocheleau

Hawaii Natural Energy Institute, University of Hawaii, 1680 East-West Road, POST 109, Honolulu, HI 96822, USA



HIGHLIGHTS

- The effects of a local GDL permeability defect on PEMFC performance were studied with a segmented cell.
- The defective GDLs through-plane gas permeabilities differed by a factor of 2.6.
- The defects were intentionally created at dimensionless flow field lengths equal to 0.4 and 0.9.
- The defect caused a change in the local performance that was more intense at high current densities.
- The higher permeability GDL improved local performance whereas the lower permeability GDL had the reverse effect.

ARTICLE INFO

Article history:

Received 12 February 2013

Received in revised form

24 April 2013

Accepted 25 April 2013

Available online 3 May 2013

Keywords:

PEMFC

Segmented cell

Spatial EIS

Gas diffusion layer

Gas permeability

Defects

ABSTRACT

The effects of local gas diffusion layer (GDL) gas permeability variation and its location on spatial and overall proton exchange membrane fuel cell (PEMFC) performance were studied using a segmented cell approach. Variations in the physical and chemical parameters of the main membrane electrode assembly's (MEA) components (e.g., the membrane, electrode, and GDL) are considered defects and might negatively affect fuel cell performance. An artificial GDL defect was introduced by exchanging a standard (or intact) cathode GDL at one segment (segment 4 or 9) with a defective GDL. The standard and defective cathode GDLs had different through-plane gas permeabilities, while values were similar for in-plane permeability and some other structural parameters. The effects from a defective GDL were observed at a high current. Introducing a highly permeable GDL as a defect increased local performance due to a decrease in mass-transfer overpotential. For a defective GDL with lower permeability than the standard GDL, a local performance decrease was observed because mass-transfer losses increased. Simultaneously, downstream segment performance improved, which might be due to changes in water management. Defect localization at the cell outlet resulted in the detection of the defect at a lower current density compared with localization at the cell inlet. Spatial polarization curves (VI) and electrochemical impedance spectroscopy (EIS) facilitated detection and localization of GDL defects. Thus it was demonstrated that the local GDL anomalies are detectable by the segmented cell system.

© 2013 Elsevier B.V. All rights reserved.

1. Introduction

The gas diffusion layer (GDL) is a membrane electrode assembly (MEA) component. It ensures electronic/heat conductivity and mechanical strength to the MEA. However, the primary GDL function is to provide water and reagent transport in proton exchange membrane fuel cells (PEMFC). The GDL must simultaneously control water transport in and out of the electrodes and set conditions for high rates of gas transport under a wide range of operating

conditions. For example, the GDL must maintain an appropriate level of membrane hydration in hot and dry environments at low currents when water production is low. On the other hand the GDL must also be adaptable to high water production rates at a high current, which facilitates efficient water removal and simultaneously directs water flow from a cathode to an anode to prevent membrane dehydration.

GDL permeability is a major parameter that influences gas and liquid transport in a PEMFC. Permeability is determined by the internal GDL structure and texture. Traditionally, a GDL comprises an electronically conductive macroporous substrate, such as carbon paper or carbon cloth, which is impregnated by a polytetrafluoroethylene (PTFE) solution to modify the hydrophobic/hydrophilic

* Corresponding author. Tel.: +1 808 593 1714; fax: +1 808 593 1719.

E-mail addresses: tatyana@hawaii.edu, t_reshetenko@mail.ru (T.V. Reshetenko).

properties. In addition, a thin microporous layer (MPL) of carbon material and PTFE is applied on the substrate. This modification provides a layered structure for the GDL, and the layers have different textural properties and pore size distributions [1,2]. Because the average MPL pore size is similar to the catalyst layers, the MPL ensures enhanced electrical contact, mechanical compatibility, as well as improved water management between a GDL and an electrode. As a result of its multi-layered structure, the GDL is highly anisotropic, and its permeability is typically represented through two values: “in-plane” (x – y direction) and “through-plane” (z direction). The viscous permeability coefficient (dimensions L^2) reflects the viscosity loss between the fluid and pore walls. The inertial permeability coefficient (dimensions L) describes losses due to changes in flow direction at the microscopic level (tortuosity) and has been combined with the viscosity loss equation of Darcy by Forchheimer (see for example [3–5]).

Most papers on GDL permeability present methods for permeability determination and its connection with GDL textural and morphological properties [3,6–9]; some studies have demonstrated the impact of gas permeability on fuel cell performance [10–15]. However, most publications that characterize GDL permeability report modeling results [16–24]. It was shown that the in-plane and through-plane permeabilities have different values, and most GDLs have higher in-plane than through-plane permeabilities because of the layered structure [3,7,10,11,15,20]. Typically, in-plane permeability does not significantly depend on an MPL; however, permeability in two perpendicular in-plane directions may produce significant anisotropy due to the direction of the aligned fibers [7]. MPL strongly impacts through-plane permeability [3,7,8,12,15,20]. The effect of an MPL on through-plane permeability confirms that textural GDL properties, such as porosity, pore volume, and pore size, determine this parameter. For example, a decrease of the GDL porosity and pore size leads to a decrease of the material permeability [10,11,13,15,17]. Based on the same reasons, GDL compression decreases through-plane permeability, as previously reported [6].

The impact of PTFE loading on a macroporous carbon substrate [8,12–14,25,26] and MPL [3,15] on GDL permeability was studied. A decrease of the GDL permeability with an increase of PTFE content was mainly reported [13–15,26]. In general, such observations are attributed to a decrease in GDL pore volume, porosity, and pore size due to infill of GDL pore volume by an excess of PTFE. However, some authors have found that an increase in PTFE loading enhances permeability [3,8,12]. The PTFE content influences GDL rigidity; materials with higher PTFE content are more rigid and therefore can crack under a compressive load. Crack formation on an MPL surface in a GDL, and hence, greater permeability was reported by M.S. Ismail et al. [8]. M. Uchida et al. [27] studied the effect of PTFE on porosity of a carbon powder–PTFE mixture. The mixture comprised 20–40 nm carbon grains, which formed larger agglomerates (200–300 nm). The pores can be classified as primary and secondary pores, respectively. The primary pores are located between the carbon grains and are 20–40 nm, whereas secondary pores are located between the carbon agglomerates, and their size ranges from 40 to 1000 nm. It was reported that the secondary pore volume increases with an increase in PTFE, whereas the primary pore volume remains unchanged [3,27]. The large PTFE particles cannot penetrate the primary pores but can penetrate the secondary pores, which increases total porosity and permeability.

The effect of GDL permeability on PEMFC performance has primarily been reported under a high current or low voltage in a limiting current region [9–15,18,24]. M.V. Williams et al. [10,11] showed a correlation between through-plane permeability and limiting current under three operating conditions, 80 °C/75% relative humidity (RH) cathode inlet, 100 °C/70% RH cathode inlet, and

120 °C/35% RH cathode inlet. GDLs with higher permeability had a higher limiting current. Moreover, it was suggested that these GDLs had larger pores and a smaller fraction of pores associated with the range affected by capillary condensation; therefore, it could avoid oxygen transport limitations due to water flooding at near-saturation conditions. G. Lin and T.V. Nguyen [12] studied the effects of GDL thickness and content of a hydrophobic agent on electrode flooding level in a PEMFC. The through-plane permeability for all the samples in this study was also measured. Higher performance was observed for GDLs with an MPL that had higher through-plane permeability.

C.-J. Tseng and S.-K. Lo [13] investigated the impact of several GDL parameters on PEMFC performance. One of the parameters was MPL thickness, which varied at 38, 84, and 136 μm . The GDL through-plane permeabilities were estimated using the semi-empirical Kozeny–Carman equation [19] as follows:

$$K = \frac{\epsilon^{n+1}}{C(1-\epsilon)^n}$$

where ϵ is porosity, while the exponent n and constant C are Kozeny–Carman constants. The through-plane gas permeability decreased with an increase in MPL thickness. However, the sample with an 84 μm MPL and an intermediate permeability value performed best at a 60 °C cell temperature and 70 °C humidifier temperature.

The impact of MPL properties on PEMFC performance was also studied in detail by T. Kitahara et al. [15]. A 110 μm -thick MPL was coated on a 24BA GDL. The MPL mean pore diameter varied from 1 to 10 μm . Through-plane permeability increased with an increase in the MPL mean pore size. Fuel cell performance was investigated at a low (0% RH) and high (100% RH) cathode humidity. Anode gas humidification was 100% RH in both cases. At low humidity the fuel cell performance was the best where the GDL had the smallest MPL pore size and lowest through-plane permeability because the MPL prevented MEA dehydration. At high humidities, the best performance was found using GDLs with a mean MPL pore diameter of 3 μm . This GDL had an intermediate through-plane permeability value as it was also reported in [13]. This GDL facilitates the transport of reagents from a gas channel to a catalyst surface as well as water transport from an electrode to the gas phase. Recent numerical analyses for PEMFCs with varying GDL permeabilities in the through-plane direction confirmed the experimental observations on the impact of permeability on PEMFC [9,18]. Water and thermal management were good in a system with high permeability in at least one direction (in-plane or through-plane), while water and heat management were poor in a system with low permeability in both directions [18].

In general, GDL permeability is connected to many GDL parameters, such as thickness, PTFE loading, compression, and MPL. Thus, permeability variation within one GDL component should be considered a defect that may affect PEMFC performance at a high current density and result in premature MEA degradation or failure. Because few papers provide experimental data for the impact of GDL permeability on a fuel cell, it is important to study effects of this GDL parameter on a PEMFC. A segmented cell system is an appropriate and powerful tool for the in-situ study of current density and voltage distributions [28–43]. The Hawaii Natural Energy Institute's (HNEI) segmented cell system was partially based on a design developed at the Los Alamos National Laboratory that used closed-loop Hall sensors [41,42] and an improved data acquisition system. This data acquisition system allows the simultaneous, rather than sequential, measurement of spatial electrochemical impedance spectroscopy (EIS), cyclic voltammetry (CV), as well as linear sweep voltammetry (LSV) to determine the

impedance response, electrochemical area (ECA), and spatial hydrogen crossover, respectively. Previously, a segmented cell system was successfully shown to serve as an excellent tool for error diagnosis in fuel cells and stacks [44–48]: such as membrane pinholes [44,45], catalyst layer variations [44], and GDL defects [46,47]. The work herein is a continuation of our previous studies of defective GDL effects on spatial PEMFC performance [46]. Previously a GDL without MPL was chosen as the defective element and the property change impact was studied with HNEI's segmented cell. A significant local performance decrease was observed at the defective area which was mainly due to a reduced electrical contact and increased ohmic losses. Additionally, the defective GDL modified mass transport at the defective area and downstream segments under high current densities. In this paper the effects of local variations in GDL gas permeability are investigated (defects at inlet and outlet sections of the MEA) and the detection capability of the segmented cell is demonstrated.

2. Experimental

All experiments were conducted using the HNEI segmented cell system and fuel cell test station described previously [42]. A simplified diagram of this system and a segmented hardware are presented in Fig. 1. This diagnostic tool enables the collection of spatial information during a standard fuel cell experiment. The segmented cell is operated as a single cell using any of the existing test stations. For the specific test station used, current and power limitations were respectively 240 A and 1.2 kW. The segmented cell system consists of the segmented cell hardware and data acquisition system, which includes a custom built current transducer

system and a National Instrument PXI data acquisition system operated by a LabView control program developed in-house (Fig. 1a). For current sensing, a closed loop Hall sensor from Honeywell, Model CSNN191 was employed. The data acquisition system is designed for measurements up to 10 current/10 voltage channels and 16 current/16 voltage channels in high or low current mode respectively. In the high current mode, which is typically used for fuel cell experiments (i.e., in H₂/air configuration), segment currents up to 2 A cm⁻² could be recorded. The low current mode yields a very accurate current measurement up to 50 mA cm⁻², which is a convenient feature for CV and LSV experiments. The PXI system data sampling frequency was 1 MHz, which was sufficient for measuring simultaneous responses from 10 segments. The hardware comprises a segmented flow field with ten cell segments that form a continuous path with ten serpentine channels. Each segment has a 7.6 cm² area and its own distinct current collector as well as GDL (Fig. 1b).

Herein, a 100 cm² Ion Power MEA with an unsegmented anode and cathode electrodes was used. Each electrode consisted of a 50% Pt/C catalyst coated on a DuPont™ Nafion® NRE 212 membrane with a 0.4 mg Pt cm⁻² load. A segmented GDL was used at the cathode, and a one-piece GDL was applied at the anode. A 25BC GDL (SGL) was used at the anode whereas GDS3215 and GDS1120 GDLs (Ballard) were used at the cathode. Tests were performed at two configurations of the cathode GDLs: when GDS3215 was the standard cathode GDL, and GDS1120 was the defective GDL; and when GDS1120 was the standard cathode GDL, and GDS3215 was the defect. Teflon gaskets 203 and 158 μ m thick were used for the anode and cathode respectively.

The primary parameters for the Ballard GDLs are listed in Table 1. GDS1120 is constructed from a P50 carbon paper substrate, while GDS3215 is based on EP40. The PTFE loading for the carbon paper substrates ranged from 8 to 15%. The GDLs have an MPL based on graphitic powder. The GDLs have similar thickness (170–175 μ m), resistance, area weight, and in-plane permeability, whereas the through-plane permeability for these GDLs is different. The GDL gas flow resistance was measured using a Gurley instrument. It was determined by the time required for 100 cm³ of air to pass through a 0.65 cm² opening under a 0.15 kg of clamping pressure. In this case the permeability ($\propto s^{-1}$) was proportional to the inverse of the Gurley ($\propto s$) values. GDS3215 has higher through-plane permeability than GDS1120 based on Gurley values (smaller values translate into larger permeabilities): respectively 80 s and 210 s leading to a ratio of 2.6. In addition, scanning electron microscope (SEM) images of the GDLs were obtained using a Hitachi S-4800 field emission SEM. The accelerating voltage for the images was 5 kV. The textural properties of the GDLs were studied by mercury intrusion porosimetry (MIP). The measurements were performed using a Micromeritics Autopore III 9410 CE.

The cell operating temperature was 60°C. The anode/cathode standard operating parameters were as follows: H₂/air, 2/2 stoichiometry, 48.3/48.3 kPa_g back pressure, and 100/50% relative humidity. Experiments were also performed with a H₂/O₂ configuration. For this test, the same flow rates as the H₂/air operation were used to maintain the cell water management. Consequently, the O₂ stoichiometry increased to 9.5. These gas configurations were used to determine segment overpotentials [42]. The activation overpotential η_{act} was obtained by subtracting the ohmic loss-corrected H₂/O₂ polarization curve from a theoretical open circuit voltage of 1.23 V. The ohmic overpotential η_{Ohm} was generated by multiplying the high frequency resistance (HFR) with the respective current density. Subtraction of the H₂/air data from the H₂/O₂ data yielded the mass-transfer overpotential η_{MT} .

The cell and segment spatially distributed voltage was measured under galvanostatic control. These experiments were combined

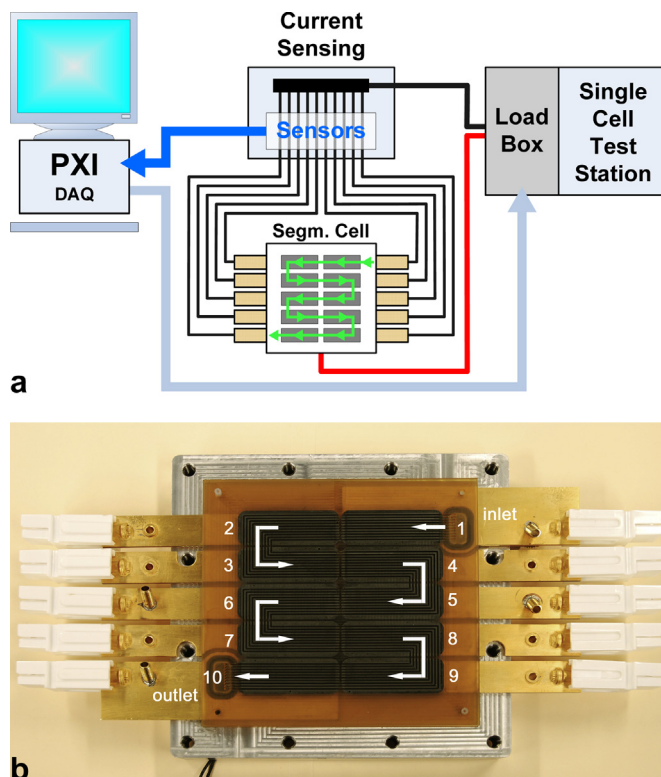


Fig. 1. Segmented cell measurement setup (a) Reprinted from Ref. [42]: T.V. Reshetenko, G. Bender, K. Bethune, R. Rocheleau, Systematic study of back pressure and anode stoichiometry effects on spatial PEMFC performance distribution, *Electrochim. Acta* 56 (2011) 8700–8710, Copyright (2011), with permission from Elsevier; segmented hardware and current collector plates (b).

Table 1

Primary parameters for the Ballard GDLs.

GDL	Carbon paper substrate	Thickness [μm]	Area weight [g m ⁻²]	PTFE [%]	Air permeability ^a [s]		Resistance [mΩ cm ²]
					Through plane	In plane	
GDS1120	P50	170	79	8–15	210	108	14.5
GDS3215	EP40	175	85	8–15	80	83	14.0

^a Permeability was determined as time required for 100 cm³ of air to pass through a 0.65 cm² opening under 0.15 kg of clamping pressure.

with EIS measurements to detect the cell and segment resistance as well as impedance spectra for all ten segments at each current. The selected EIS frequency range was 0.1 Hz–10 kHz, and the sinusoidal current signal amplitude perturbation was 2 A, which produced a cell voltage response of 10 mV or less. The HFR was determined from the intercept of the EIS curve with the real impedance axis at high frequencies (Nyquist plot).

The CV experiments were conducted to measure the electrochemically active surface area (ECA) using a Parstat 2273 potentiostat/galvanostat from EG&G Instruments Corp. The CVs were performed at 35°C cell temperature with 20 mV s⁻¹ scan rate, while 100% relative humidity hydrogen and nitrogen were supplied to the reference/counter and working electrodes, respectively, at a 750 ml min⁻¹ flow rate. For each measurement, three cycles were recorded over a –0.015 to 1.1 V potential range compared with the hydrogen reference electrode (HRE). The hydrogen desorption peak area from the third cycle was used to determine the ECA. Hydrogen crossover experiments were performed at the same temperature and flow conditions as the ECA measurements using a single potential sweep from 0.1 to 0.4 V compared with the HRE at a 0.1 mV s⁻¹ scan rate.

The GDL defects were created by exchanging the standard cathode GDL (GDS3215) material at segment 4 and segment 9 with a substitute GDL (GDS1120). For the opposite GDL configuration test, the standard GDL (GDS1120) at segment 4 was exchanged for GDS3215. The defect simulated the different air permeability expected from manufacturing. Prior to defect insertion, the segmented cell was assembled using a standard GDL, and a series of diagnostics was performed. For the diagnoses, a CV was used to determine the electrode ECA; an LSV was used to determine the hydrogen crossover current for the cell; and analysis of the VI curves as well as spatial EIS with the H₂/air and H₂/O₂ gas configurations was used to determine the performance and overpotential distributions of the cell as well as the impedance spectra. The cell was subsequently disassembled, the defect inserted, the cell reconditioned, and an identical set of diagnostics were completed. A comparison of the diagnostics provided insight into the defect effects.

3. Results and discussion

3.1. Performance comparison for GDS1120 and GDS3215

The performances for two MEAs with different cathode GDLs (GDS1120 and GDS3215 at all segments) are presented in Fig. 2, which shows spatial VI curves for segments 1, 4, 7, and 10 as well as the entire cell. The results for these four segments represent the trends observed for the whole cell. The main difference in the performances for these MEAs was observed at a high current density. For GDS1120, the limiting current was reached by the segments and the cell. However, the MEA with GDS3215 did not reach the limiting current. The GDL through-plane permeability reportedly correlates with cell performance, and an increase in GDL gas permeability causes an increase in the limiting current [10,12,13,15].

In-plane and through-plane permeability values greatly depend on several GDL parameters (e.g., thickness, density, hydrophobic agent loading, fiber structure, and an MPL presence) [49]. GDS1120 and 3215 are similar in thickness and have MPL coating. SEM studies of these GDLs (Fig. 3) demonstrate that carbon papers are the macroporous substrate, but GDS1120 has more close structure on the carbon paper (Fig. 3a–d) and MPL sides (Fig. 3e, f) compared with GDS3215. The MIP data are consistent with the SEM results (Fig. 4, Table 2).

The GDS3215 has higher porosity and total pore volume compared with GDS1120 (2.0308 vs. 1.5473 cm³ g⁻¹). Pore size distribution (PSD) curves distinguish several pore size regions: large pores (25–150 μm), medium (1–25 μm), and fine pores (0.1–1 μm) (Fig. 4a). GDS1120 has a higher volume of fine pores, while GDS3215 is characterized by greater volumes of medium and large pores (Fig. 4b). Thus, there is a correlation between the diffusion media textural properties and permeability. GDS3215 has larger pores, and a smaller pore volume fraction could be affected by capillary condensation [10,12]. When the pore size gets smaller than a certain critical diameter, water will condense before the vapor pressure reaches the saturation pressure at a given temperature. Therefore, small pores will be filled by water even when the relative humidity is less than 100%. The water vapor pressure for condensation depends on the pore diameter according to the following Kelvin equation [50]:

$$\ln \frac{P}{P_0} = -\frac{2\gamma V_L}{RT} \cdot \frac{1}{r_m}$$

P/P_0 is the relative pressure of vapor in equilibrium with a meniscus and has a radius of curvature r_m ; γ and V_L are the surface tension and molar volume, respectively, for the liquid adsorbate. R and T are gas constant and temperature. The higher the permeability, the smaller the fraction of volume affected by capillary condensation, and the less likely oxygen transport is limited by water flooding at near-saturation conditions.

In a GDL, gas diffuses through bulk and Knudsen diffusion depending on mean-free path, which determines whether the collision between gas molecules or pore walls is dominant. Under standard conditions, the mean-free path of air is approximately 70 nm. Bulk diffusion in pores dominates when the pore diameter is greater than one hundred times the mean-free path (~7 μm), while Knudsen diffusion dominates when the pore diameter is smaller than one tenth of the mean-free path (~7 nm). Pores between 7 μm and 7 nm will have combined bulk and Knudsen diffusion properties [10]. For oxygen diffusion, larger pores are beneficial because they aid bulk diffusion, which is more important than Knudsen in gas transport through the GDL. However, the small pores that are typically located in the MPL are very important for water transport from a catalyst layer to a gas channel because they reduce water vapor saturation and prevent catalyst layer flooding due to capillary pressure [51,52]. Thus, large and small pores in the GDL are a reasonable compromise for providing good oxygen and water transport simultaneously. Because the through-plane permeability for GDS1120 is 2.6 times lower than GDS3215 (Table 1), the MEA sample with GDS1120 has higher mass-transfer overpotential,

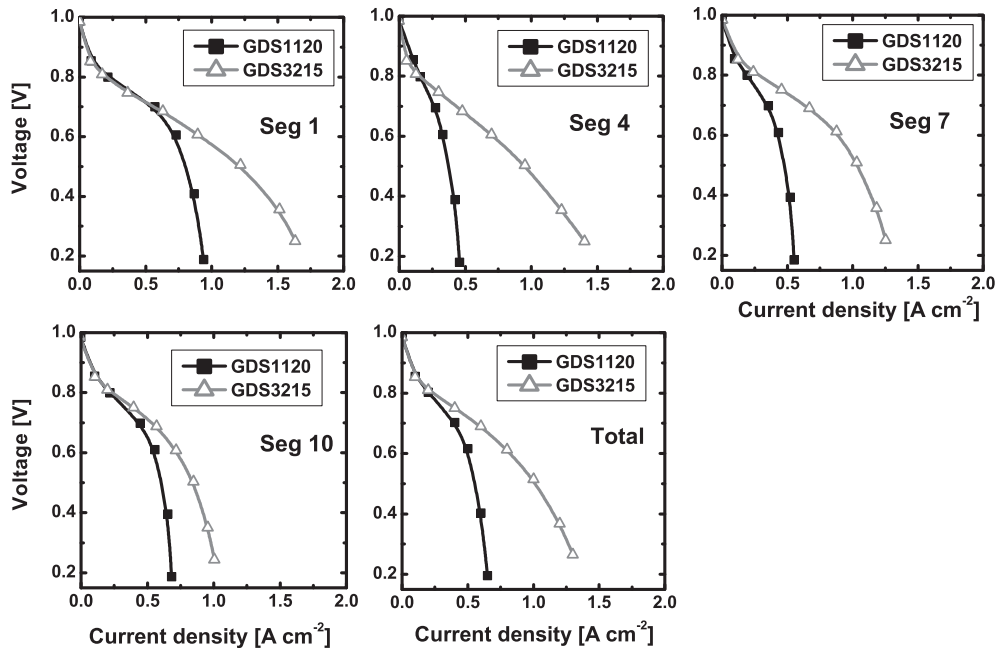


Fig. 2. VI curves for segments 1, 4, 7, and 10 as well as the entire cell. Anode/cathode: H_2/air , 2/2 stoichiometry, 100/50% RH, 48.3/48.3 kPa_g, and 60 °C.

which explains the observed performances. A detailed analysis of the overpotentials will be discussed in the following chapters.

3.2. Impact of the defect on the ECA and H₂-crossover

Analysis of the ECA before and after introducing the defect showed that the ECA uniformly decreased at all segments for both the anode and cathode in each test described below. The 3–7% decreased ECA might be explained by catalyst degradation during disassembly of the hardware, exposure of the catalyst to air, and degradation during cell operation. However, because this effect was observed throughout the entire cell and not exclusively at the defective segment, it did not impact the analysis of a local GDL defect. Comparing the H₂-crossover distributions showed no pinhole formations during the defect introduction.

3.3. GDL with high gas permeability as a defect at segment 4

For this experiment, GDS1120 with low permeability was used as a standard cathode GDL, while GDS3215 with high permeability was the defective GDL. The influence of this GDL defect on fuel cell performance distribution is shown in Fig. 5a, which depicts the voltage distributions of the cell as a function of the segment locations for different constant current densities. It should be noted that the initial performance of the MEA with GDS1120 cathode GDL was lower than with GDS3215 (Fig. 2); therefore, the voltage distributions are presented only at low current densities 0.1, 0.2, and 0.4 A cm⁻². The defective highly gas permeable GDL had a positive impact on local performance, as previously reported [10–13,15]. The performance at segment 4 was increased by 0.033 and 0.205 V at 0.2 and 0.4 A cm⁻², respectively. There is a variation of the downstream segments performance at 0.4 A cm⁻² after the defect introduction (for example, segment 8 in Fig. 5a). Such deviation is likely not caused by the defective GDL at segment 4 and might be explained by the fact that current densities of the outlet segments approached limiting current values. The cell performance distributions are obtained from segments' polarization curves by replotting individual segments voltages at constant current

densities. As an example, Fig. 5b presents polarization curves for segments 1, 4, 7, 10, and the entire cell. The initial performance of segment 4 with GDS1120 was slightly lower than other segments and was most likely ascribed to variations in local mass-transport, which is also reflected in performance distribution (Fig. 5a). The defective GDS3215 significantly improved the local performance at high current densities, shifted the segment's limiting current to a larger value (from 0.45 to 0.62 A cm⁻²), and proved the positive impact of a highly permeable GDL. The defective GDL did not noticeably modify the performance of the other segments as well as the entire cell, although a slight performance increase was noted for the overall cell at ~0.65 A cm⁻² (Fig. 5b).

The data were analyzed further by determining the distributions of the activation, ohmic, and mass-transfer overpotentials [42], and they indicate that the primary contributor to performance change at segment 4 is mass-transfer overpotential. Fig. 5c shows the change in the mass-transfer overpotential distribution for the defective and standard MEA with current densities from 0.1 to 0.4 A cm⁻². An increase in air permeability at segment 4 decreased the mass-transfer losses. The overpotential drop was 0.028 and 0.200 V at 0.2 and 0.4 A cm⁻², respectively, which corresponds to approximately 90% of the performance change.

The performance data are supported by EIS results. Fig. 6 shows the EIS spectra for segments 1, 4, 7, and 10 recorded at 0.1 and 0.4 A cm⁻² overall current density before and after introduction of the defect at segment 4. The results for these four segments are representative of the trends observed in the entire cell. The impedance spectra for segments 1–3 recorded at low current density (Fig. 6a) included several arcs: a high-frequency anode arc (typically this arc is negligible, but it was noticeable at a low current density), a high-frequency cathode arc attributed to the charge-transfer resistance and the double-layer capacitance of the cathode catalyst [53]. The membrane and the electronic contact resistance determine the HFR for the MEA. For segments 4–10, the low-frequency arc is clearly observable, which reflects the mass-transfer (or diffusion) limitation within the GDL and the catalyst layer at 0.1 A cm⁻². At a low current density operation, no changes were detected in the EIS responses after the defect was introduced at

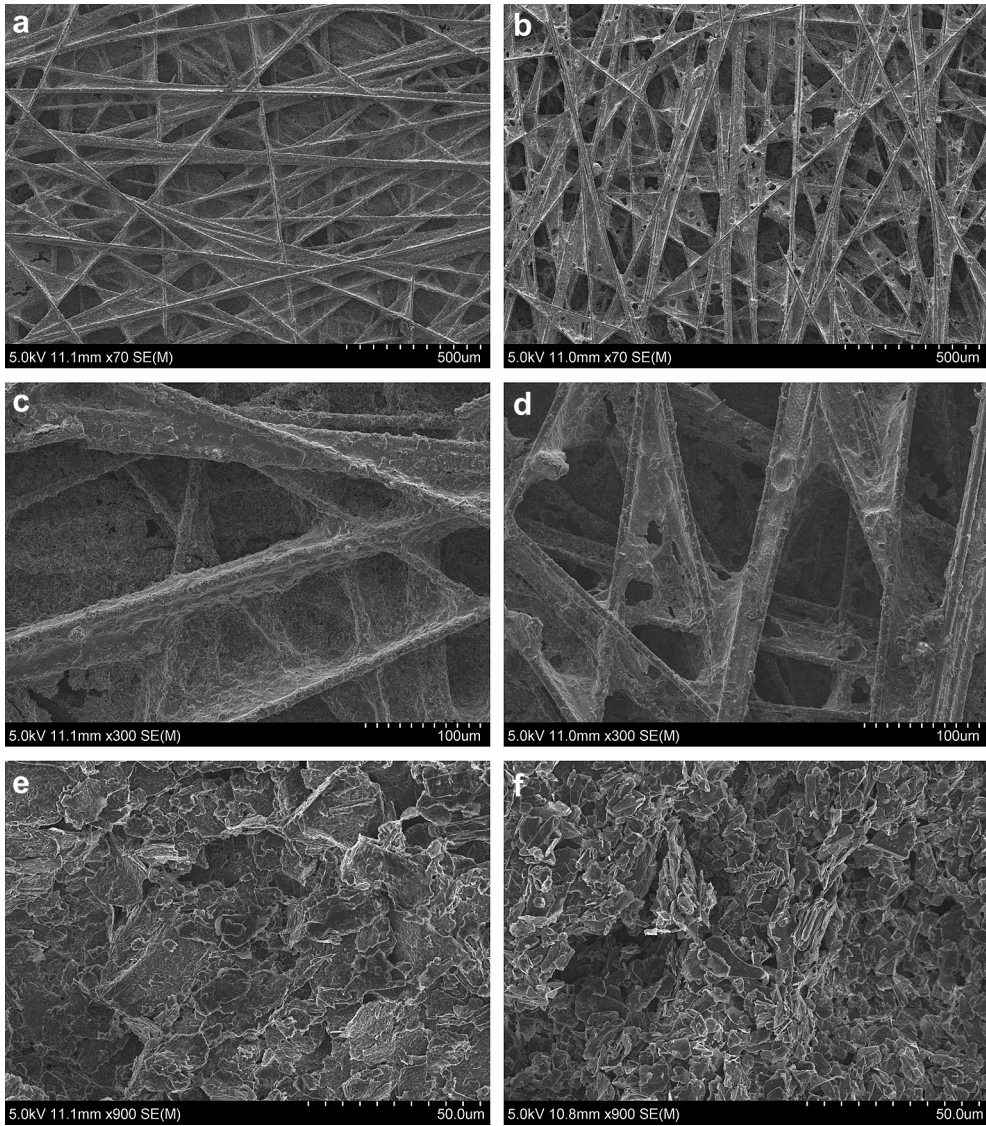


Fig. 3. SEM images for GDS1120 (a, c – carbon paper side; and e – MPL side) and GDS3215 (b, d – carbon paper side; and f – MPL side).

segment 4 (Fig. 6a), aside from a slight decrease in HFR from 0.199 to $0.180 \Omega \text{ cm}^2$, which was likely due to MPL properties in the GDL. However, at 0.4 A cm^{-2} , segment 4 had a decreased low-frequency arc after changing the GDL, which indicated an improved local mass-transfer properties due to an increase in air permeability for

the defective GDL (Fig. 6b). After introducing the defect, the low-frequency arc diameter was slightly enhanced for segments 7–10. This finding might be explained by a low voltage operation and more sensitive EIS than polarization measurements facilitating the detection of small deviations in the performance.

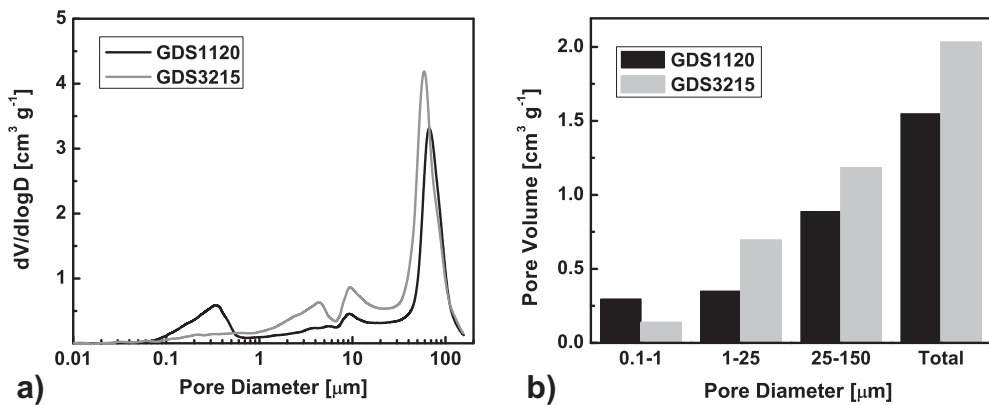


Fig. 4. Pore size distributions for the GDLs (a) and pore volumes for regions with different pore sizes (b).

Table 2

Textural properties of the GDS1120 and 3215 obtained by MIP.

GDL	Porosity [%]	Pore volume $25\text{--}150\text{ }\mu\text{m}$ [$\text{cm}^3\text{ g}^{-1}$]	Pore volume $1\text{--}25\text{ }\mu\text{m}$ [$\text{cm}^3\text{ g}^{-1}$]	Pore volume $0.1\text{--}1\text{ }\mu\text{m}$ [$\text{cm}^3\text{ g}^{-1}$]	Pore volume [$\text{cm}^3\text{ g}^{-1}$]
GDS1120	72.99	0.8864	0.3491	0.295	1.5473
GDS3215	74.95	1.1829	0.6936	0.1374	2.0308

3.4. GDL with low gas permeability as a defect at segment 4

For this experiment, the highly permeable GDS3215 cathode GDL was used as a standard, while the GDS1120 with low permeability was used as the defective GDL at segment 4. Fig. 7a shows fuel cell performance distributions before and after introducing the defect in terms of voltage distributions as a function of segment location for different constant current densities. The results indicate that higher current densities operation ($\geq 1.0\text{ A cm}^{-2}$) facilitate the defect detection [10–15]. The segment 4 voltage decreased after the defect was introduced by 0.039 V at 1.0 A cm^{-2} , 0.09 V at 1.1 A cm^{-2} , and 0.160 V at 1.2 A cm^{-2} . The defect affected segment performance downstream at high current density operations:

segments 5–10 increased in performance (Fig. 7a), but the overall cell performance was not affected by the introduction of the defect (Fig. 7b).

Overpotential data indicated that the primary contributor to performance in segment 4 was mass-transfer loss (Fig. 7c). The overpotential increase was 0.022, 0.083, and 0.132 V at 1.0 , 1.1 and 1.2 A cm^{-2} , respectively. Furthermore, the HFR increased at the defective location from 0.208 to $0.245\text{ }\Omega\text{ cm}^2$, which generated a slight increase in local ohmic loss, 0.017, 0.025, and 0.028 V at 1.0 , 1.1 , 1.2 A cm^{-2} , respectively. The ohmic and mass-transfer overpotentials sum accounts for 99% of the performance loss.

Fig. 8 shows EIS data collected at an entire cell current density of 0.1 and 1.0 A cm^{-2} for segments 1, 4, 7, and 10 before and after defect introduction at segment 4. At a low current density (0.1 A cm^{-2}), local changes in GDL air permeability were not detectable; therefore, this defect does not affect cathode charge transfer resistance. However, a slight increase in HFR was observed (Fig. 8a). Such an increase in HFR might be connected to cell assembly/disassembly and/or different adhesive properties of the GDL MPL. At a high current density operation (1.0 A cm^{-2}), the defect increased the low-frequency loop at segment 4 (Fig. 8b), which represents diffusion limitations within the GDL and catalyst

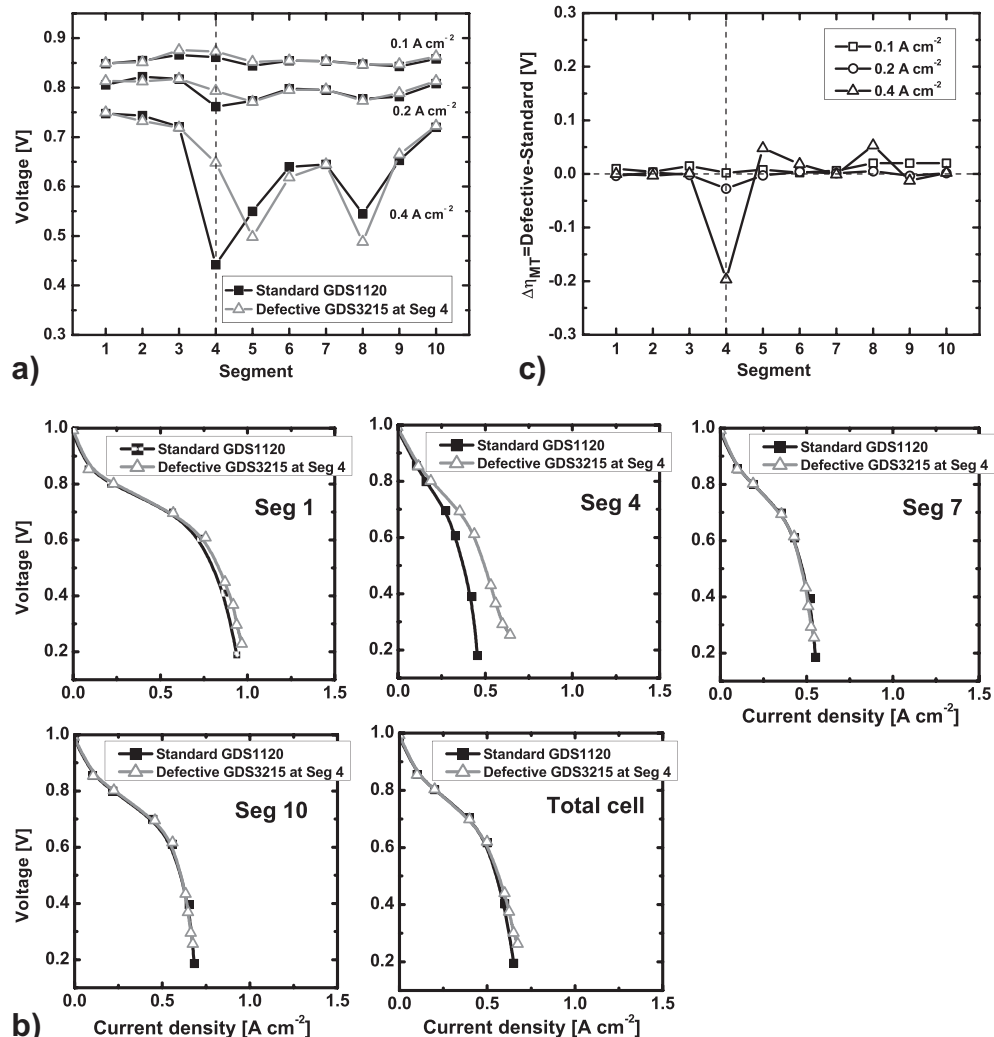


Fig. 5. Voltage distributions for MEA with a standard GDL (GDS1120) and a defective GDL (GDS3215) at segment 4 (a). Polarization curves for segments 1, 4, 7, 10, and the total cell before and after introduction of the defect at segment 4 (b). Anode/cathode: H_2/air , 2/2 stoichiometry, 100/50% RH, $48.3/48.3\text{ kPa}_\text{g}$ and 60°C . Differential distributions of the mass-transfer overpotentials for the MEA with the defective GDL at segment 4 and the standard GDL (c). The defect position is indicated by a dashed line.

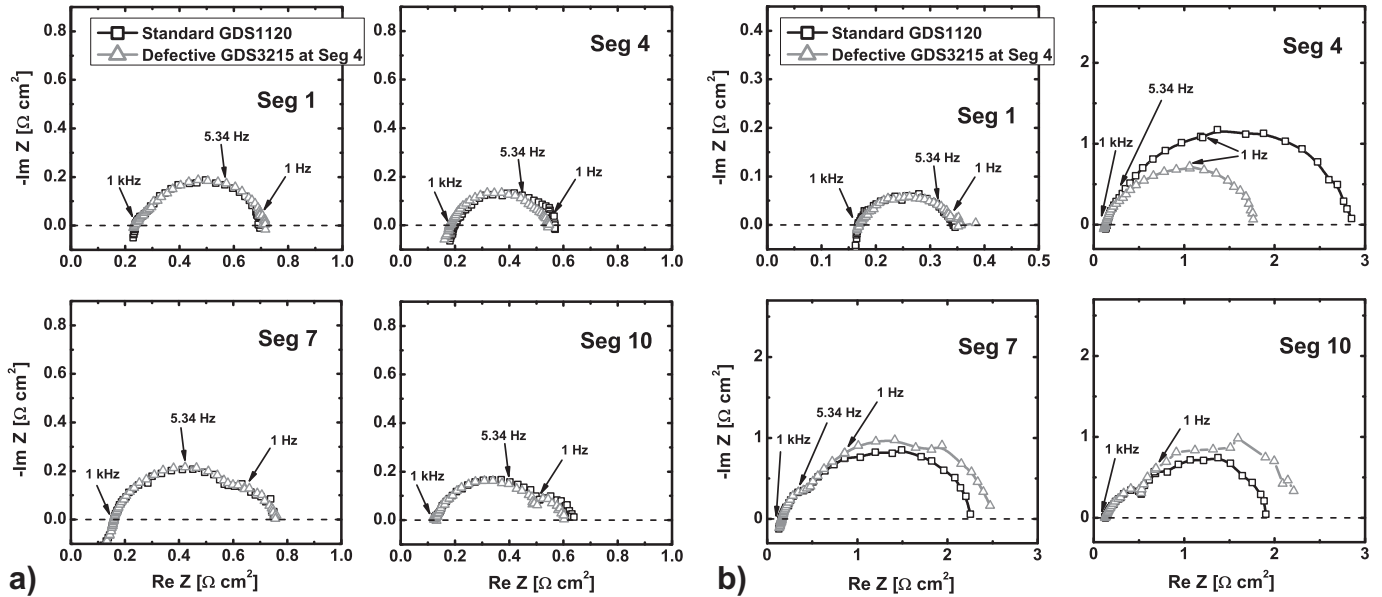


Fig. 6. EIS spectra for segments 1, 4, 7, and 10 recorded at an overall cell current density $i = 0.1$ (a) and 0.4 A cm^{-2} (b) before and after the defect was introduced at segment 4. Anode/cathode: H_2/air , 2/2 stoichiometry, 100/50% RH, 48.3/48.3 kPa_g, and 60 °C.

layer due to poor mass transport. Simultaneously, the downstream segments demonstrated a decrease in diffusion loop size and an increase in performance.

A decrease in the local GDL air permeability results in an increase of the local mass-transfer because oxygen and water transport through the GDL is difficult at high current density operation.

This creates conditions for oxygen diffusion limitations as well as water flooding at the defective area and local decrease in performance. As the local performance decreases, water removal from the defected segment is an obstacle, so less water is emitted downstream, which produces dry conditions for the segments downstream of the defect, thus improving the downstream performance.

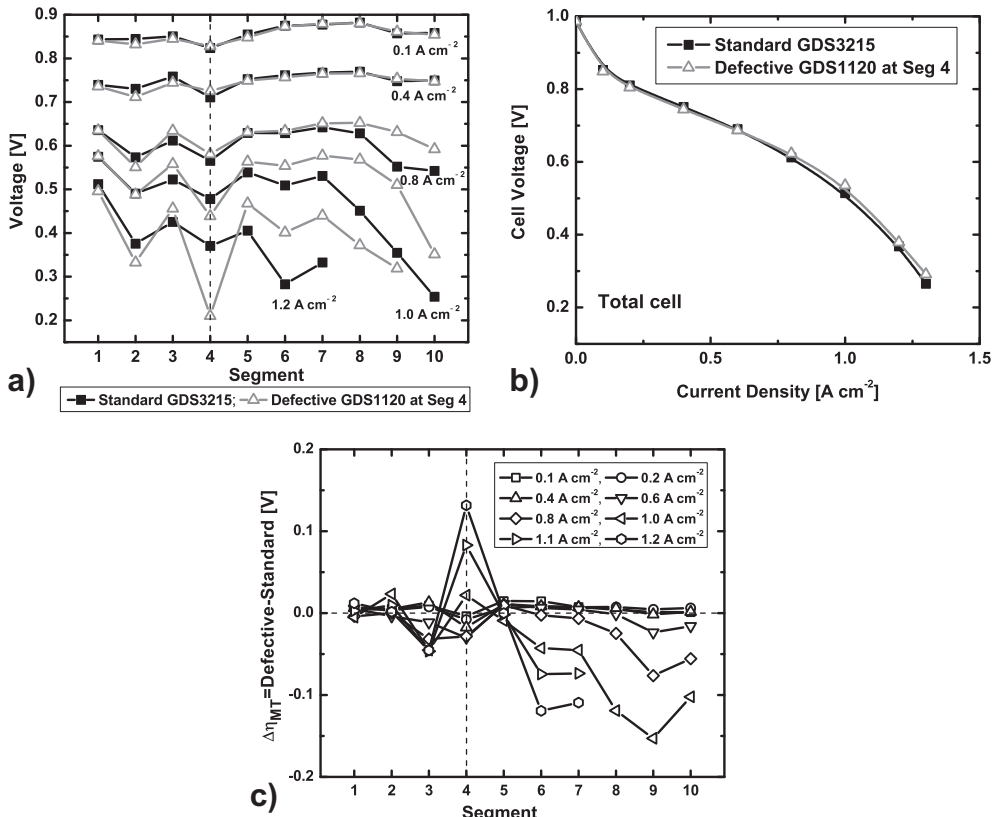


Fig. 7. Voltage distributions for the MEA with a standard GDL (GDS3215) and a defective GDL (GDS1120) at segment 4 (a). Polarization curves for the total cell before and after the defect was introduced at segment 4 (b). Anode/cathode: H_2/air , 2/2 stoichiometry, 100/50% RH, 48.3/48.3 kPa_g, and 60 °C. Differential distributions of the mass-transfer overpotentials for the MEA with the defective GDL at segment 4 and the standard GDL (c). The defect position is indicated by a dashed line.

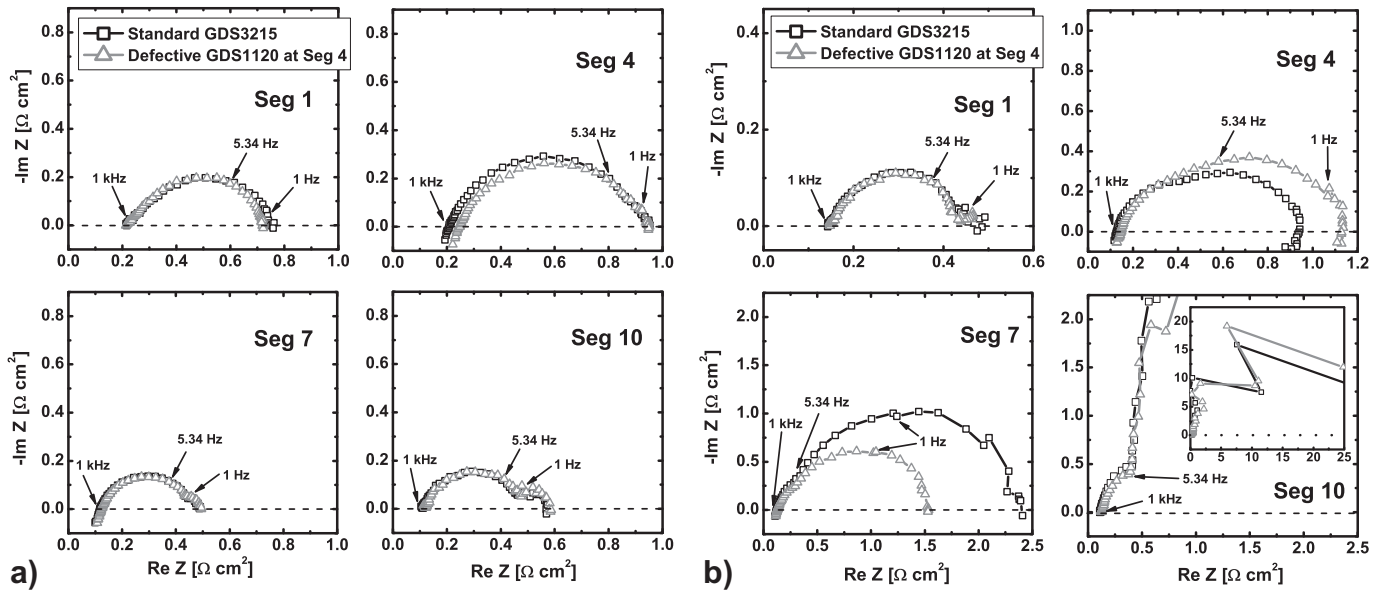


Fig. 8. An EIS spectra for segments 1, 4, 7, and 10 recorded at an overall cell current density $i = 0.1$ (a) and 1.0 A cm^{-2} (b) before and after introduction of GDS1120 as the GDL defect at segment 4. Anode/cathode: H_2/air , 2/2 stoichiometry, 100/50% RH, 48.3/48.3 kPa_g, and 60 °C.

3.5. GDL with low gas permeability as a defect at segment 9

To study the impact of defect location, we replaced the defective GDS1120 at segment 4 with the standard GDS3215 and introduced a defect (GDS1120) at segment 9. **Fig. 9a** shows the voltage distributions as a function of segment position before and after

introduction of the defective GDL at segment 9. The primary impact of the defect on performance was observed at high current density operation. A decrease in local air permeability produced a local performance decrease of 0.034 and 0.23 V at 0.8 and 0.9 A cm^{-2} , respectively. Simultaneously, the performance of segments 6–8 and 10 increased. The defect did not cause significant changes in VI

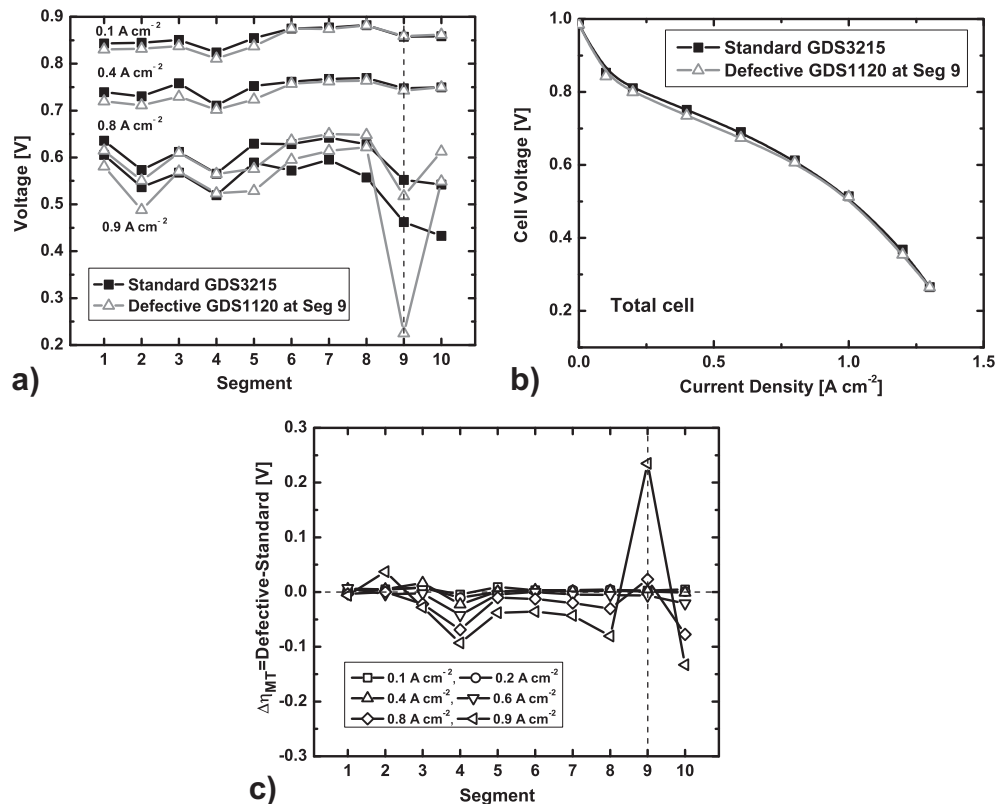


Fig. 9. Voltage distributions for the MEA with a standard GDL (GDS3215) and a defective GDL (GDS1120) at segment 9 (a). Polarization curves for the total cell before and after the defect was introduced at segment 9 (b). Anode/cathode: H_2/air , 2/2 stoichiometry, 100/50% RH, 48.3/48.3 kPa_g, and 60 °C. Differential distributions of the mass-transfer overpotentials for the MEA with the defective GDL at segment 9 and the standard GDL (c). The defect position is indicated by a dashed line.

behavior for the entire cell (Fig. 9b). The observed local performance decrease is primarily due to an increase of the mass-transfer losses, as indicated in Fig. 9c. The growth of this overpotential is 0.025 and 0.234 V at 0.8 and 0.9 A cm⁻², respectively, which corresponds to 95% of the performance decrease.

Fig. 10 presents EIS spectra for segments 1, 2, and 7–10 recorded at 0.1 and 1.0 A cm⁻² total current density before and after defect introduction at segment 9. At a low current density (Fig. 10a), the air permeability defect did not significantly impact the impedance of the segments, as found in the previous case. The previously observed increase in HFR was the same for segment 9; HFR increased from 0.108 to 0.120 Ω cm². At a high current density, EIS showed changes in the behavior of segment 9 (Fig. 10b).

The low-frequency loop size was increased, which became negative and was located in quadrant II of the Nyquist plot. Such EIS behavior may be explained by mass-transfer limitations and O₂ depletion [39].

Comparing the impact of the defect location (segment 4 vs. segment 9) shows that the defect at the cell outlet (segment 9) was more pronounced and produced a critical performance decrease at a lower current than the defect located at the cell inlet (segment 4) (Figs. 7a and 9a). The defect was detected at 1.1–1.2 A cm⁻² for the inlet location and 0.8–0.9 A cm⁻² for the outlet location. Typically, the outlet segments suffer from oxygen depletion in the gas phase and during water accumulation [39,42,43], and introducing the permeability defect aggravates existing mass-transfer limitations.

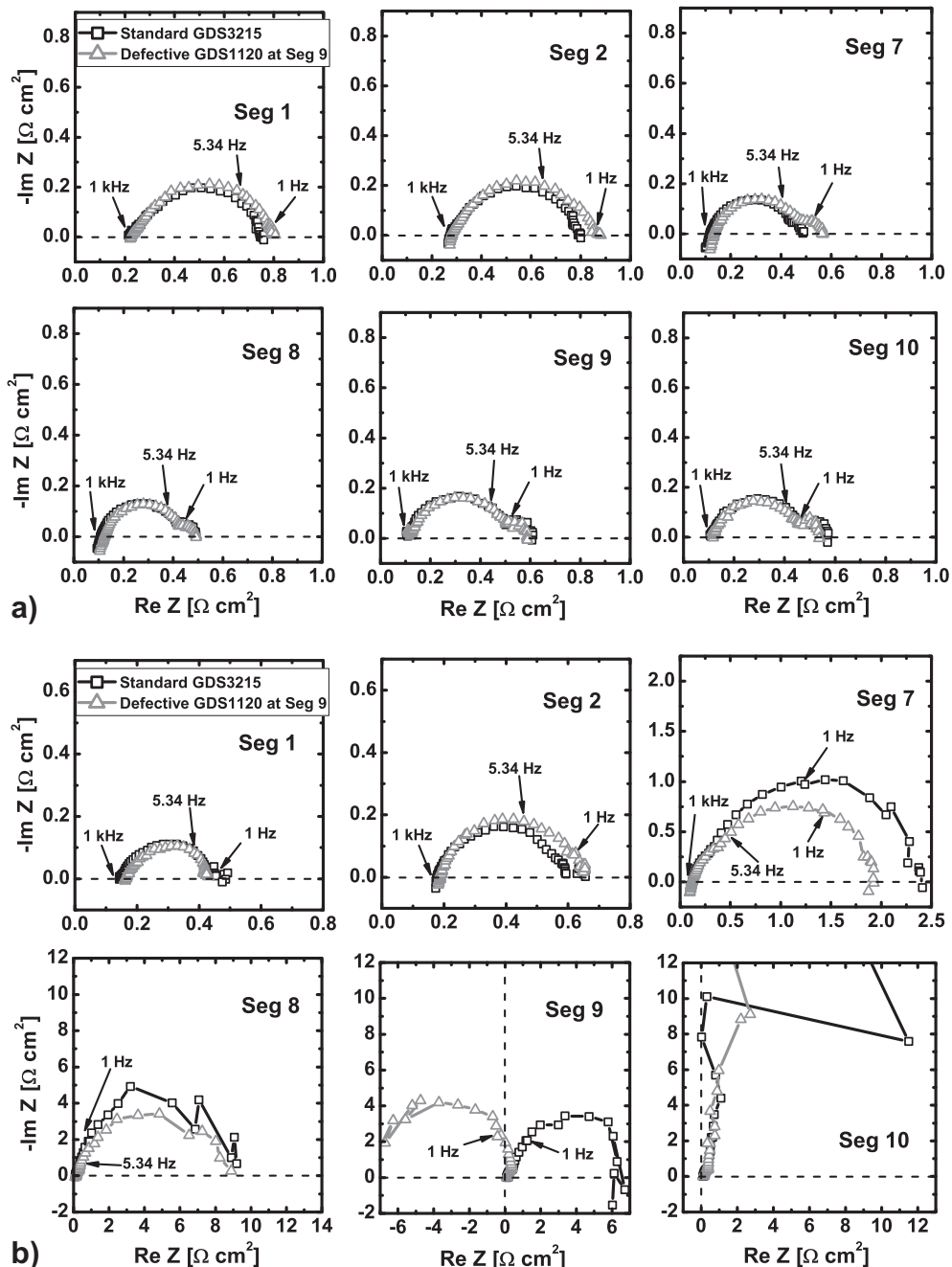


Fig. 10. The EIS spectra for segments 1, 2, and 7–10 recorded at overall cell current density $i = 0.1$ (a) and 1.0 A cm^{-2} (b) before and after introduction of GDS1120 as the defective GDL at segment 9. Anode/cathode: H₂/air, 2/2 stoichiometry, 100/50% RH, 48.3/48.3 kPa_g, and 60°C.

4. Conclusion

In this work, the effect of variations in GDL gas permeability on spatial PEMFC performance was studied using a segmented cell system. Two GDLs with distinctly different through-plane gas permeabilities (high and low values) were used. The variation in local cathode GDL permeability was considered a defect and was artificially created by exchanging a standard GDL at one segment (segment 4 or 9) with a substitute defective GDL. The results showed that the defect mainly affected local performance at high current operation.

The data indicate that cathode GDL gas permeability primarily affects mass-transfer overpotential. Spatial VI and EIS data showed that when the defective GDL was highly permeable compared with a standard GDL, performance increased at the defective area due to a local decrease in the mass-transfer overpotential. If the defective GDL had low permeability compared with the standard cathode GDL, it caused a local performance decrease and simultaneously improved the performance of the downstream segments because of an increase in mass-transfer overpotential at the defective segment and modified water management downstream. Studies on the defective location indicated that defects at the cell outlet are pronounced and detectable at lower currents compared with defects at the cell inlet. The preferred methods for detection of GDL defects were a combination of spatial VI measurements and EIS. Results have demonstrated that a segmented cell system is a powerful tool to detect GDL permeability defects and contributed to the expansion of the existing list of detectable defects [44,46].

The local variations in GDL properties did not significantly affect overall cell performance (Figs. 5b, 7b, and 9b). Thus, introducing a 10% defective cathode GDL area did not modify the entire cell performance that brings about a question regarding the critical defect size, which might affect the total cell activity. Moreover, local permeability variations caused highly inhomogeneous performance distributions (Figs. 5a, 7a, and 9a) and formed areas that have a decreased performance and might cause premature failure for long-term cell operation due to significant local flooding, catalyst degradation, and possible local heating. Therefore, future studies on the impact of defects and defect size on long-term PEMFC operation are necessary for manufacturing reliable MEAs.

Acknowledgments

We would like to acknowledge Günter Randolph (Grandalytics) for a valuable support on the segmented cell system and software; Julie Bellerive (Ballard Power System) for MIP data on the GDLs; Jason Morgan (Ballard Material Products) for certain GDL property data. We are grateful to the Hawaiian Electric Company for their ongoing support to the operations of the Fuel Cell Test Facility.

References

- [1] L. Cindrella, A.M. Kannan, J.F. Lin, K. Saminathan, Y. Ho, C.W. Lin, J. Wertz, *J. Power Sources* 194 (2009) 146–160.
- [2] M. Mathias, J. Roth, J. Flemming, W. Lehnert, *Diffusion Media Materials and Characterization*, in: W. Vielstich, H.A. Gasteiger, A. Lamm (Eds.), *Handbook of Fuel Cell – Fundamentals, Technology and Applications*, Fuel Cell Technology and Applications. Part 1, vol. 3, John Wiley and Sons, Weinheim, 2003, pp. 517–537. (Chapter 42).
- [3] V. Gurau, M.J. Blumele, E.S. De Castro, Y.-M. Tsou, T.A. Zawodzinski Jr., J.A. Mann Jr., *J. Power Sources* 165 (2007) 793–802.
- [4] A. Bejan, *Convection Heat Transfer*, John Wiley & Sons, 1984.
- [5] M.M. Tomadakis, T.J. Robertson, *J. Compos. Mater.* 39 (2005) 163–188.
- [6] J.P. Feser, A.K. Prasad, S.G. Advani, *J. Power Sources* 162 (2006) 1226–1231.
- [7] J.T. Gostick, M.W. Fowler, M.D. Pritzker, M.A. Ioannidis, L.M. Behra, *J. Power Sources* 162 (2006) 228–238.
- [8] M.S. Ismail, D. Borman, T. Damjanovic, D.B. Ingham, M. Pourkashanian, *Int. J. Hydrogen Energy* 36 (2011) 10392–10402.
- [9] G. Inoue, Y. Matsukuma, M. Minemoto, *J. Power Sources* 157 (2006) 153–165.
- [10] M.V. Williams, E. Begg, L. Bonville, H.R. Kunz, J.M. Fenton, *J. Electrochem. Soc.* 151 (2004) A1173–A1180.
- [11] M.V. Williams, H.R. Kunz, J.M. Fenton, *J. Electrochem. Soc.* 151 (2004) A1617–A1627.
- [12] G. Lin, T.V. Nguyen, *J. Electrochem. Soc.* 152 (2005) A1942–A1948.
- [13] Ch.-J. Tseng, Sh.-K. Lo, *Energy Convers. Manag.* 51 (2010) 677–684.
- [14] M. Prasanna, H.Y. Ha, E.A. Cho, S.-A. Hong, I.-H. Oh, *J. Power Sources* 131 (2004) 147–154.
- [15] T. Kitahara, T. Konomi, H. Nakajima, *J. Power Sources* 195 (2010) 2202–2211.
- [16] G. He, Z. Zhao, P. Ming, A. Abuliti, C. Yin, *J. Power Sources* 163 (2007) 846–852.
- [17] A. Tamayol, M. Bahrami, *J. Power Sources* 196 (2011) 3559–3564.
- [18] D.H. Ahmed, H.J. Sung, J.M. Bae, *Int. J. Hydrogen Energy* 33 (2008) 3767–3785.
- [19] Y. Shi, J. Xiao, M. Pan, R. Yuan, *J. Power Sources* 160 (2006) 277–283.
- [20] J.G. Pharaoh, *J. Power Sources* 144 (2005) 77–82.
- [21] W. Sun, B.A. Peppley, K. Karan, *J. Power Sources* 144 (2005) 42–53.
- [22] J. Zou, X.-F. Peng, W.-M. Yan, *J. Power Sources* 159 (2006) 514–523.
- [23] Z. Shi, X. Wang, *J. Power Sources* 185 (2008) 985–992.
- [24] G. Lin, T.V. Nguyen, *J. Electrochem. Soc.* 153 (2006) A372–A382.
- [25] D. Bevers, R. Rogers, M. von Bradke, *J. Power Sources* 63 (1996) 193–201.
- [26] G.-G. Park, Y.-J. Sohn, T.-H. Yang, Y.-G. Yoon, W.-Y. Lee, Ch.-S. Kim, *J. Power Sources* 131 (2004) 182–187.
- [27] M. Uchida, Y. Aoyama, N. Eda, A. Ohta, *J. Electrochem. Soc.* 142 (1995) 4143–4149.
- [28] J. Wu, X.Z. Yuan, H. Wang, M. Blanco, J.J. Martin, J. Zhang, *Int. J. Hydrogen Energy* 33 (2008) 1747–1757.
- [29] X. Yuan, H. Wang, J.C. Sun, J. Zhang, *Int. J. Hydrogen Energy* 32 (2007) 4365–4380.
- [30] Ch. Wieser, A. Helmbold, E. GÜLZOW, *J. Appl. Electrochem.* 30 (2000) 803–807.
- [31] L.C. Pérez, L. Brandão, J.M. Sousa, A. Mendes, *Renew. Sustain. Energy Rev.* 15 (2011) 169–185.
- [32] S. Cleghorn, C.R. Derouin, M.S. Wilson, S. Gottesfeld, *J. Appl. Electrochem.* 28 (1998) 663–672.
- [33] J. Stumper, S.A. Campbell, D.P. Wilkinson, M.C. Johnson, M. Davis, *Electrochim. Acta* 43 (1998) 3773–3783.
- [34] M. Noponen, T. Mennola, M. Mikkola, T. Hottinen, P. Lund, *J. Power Sources* 106 (2002) 304–312.
- [35] J.J. Hwnag, W.R. Chang, R.G. Peng, P.Y. Chen, A. Su, *Int. J. Hydrogen Energy* 33 (2008) 5718–5727.
- [36] Y.-G. Yoon, W.-Y. Lee, T.-H. Yang, G.-G. Park, Ch.-S. Kim, *J. Power Sources* 118 (2003) 193–199.
- [37] N. Rajalakshmi, M. Raja, K.S. Dhathathreyan, *J. Power Sources* 112 (2002) 331–335.
- [38] F.-B. Weng, B.-Sh. Jou, Ch.-W. Li, A. Su, Sh.-H. Chan, *J. Power Sources* 181 (2008) 251–258.
- [39] I.A. Schneider, S.A. Freunberger, D. Kramer, A. Wokaun, G.G. Scherer, *J. Electrochem. Soc.* 154 (2007) B383–B388.
- [40] I.A. Schneider, D. Kramer, A. Wokaun, G.G. Scherer, *J. Electrochem. Soc.* 154 (2007) B770–B782.
- [41] G. Bender, M.S. Wilson, T.A. Zawodzinski, *J. Power Sources* 123 (2003) 163–171.
- [42] T.V. Reshetenko, G. Bender, K. Bethune, R. Rocheleau, *Electrochim. Acta* 56 (2011) 8700–8710.
- [43] T.V. Reshetenko, G. Bender, K. Bethune, R. Rocheleau, *Electrochim. Acta* 69 (2012) 220–229.
- [44] T.V. Reshetenko, G. Bender, K. Bethune, R. Rocheleau, *Electrochim. Acta* 76 (2012) 16–25.
- [45] R. Lin, E. GÜLZOW, M. Schulze, K.A. Friedrich, *J. Electrochem. Soc.* 158 (2011) B11–B17.
- [46] T.V. Reshetenko, G. Bender, K. Bethune, R. Rocheleau, *Electrochim. Acta* 80 (2012) 368–376.
- [47] R. Borup, R. Mukundan, J. Davey, J. Spendelow, P. Mukherjee, D. Wood, M. Nelson, F. Garzon, M. Arif, D. Jacobson, D. Hussey, *In Situ PEM Fuel Cell Water Managements, LRD42b-3, 2009 Fuel Cell Seminar* (16–19 November 2009), Palm Springs, CA, USA.
- [48] M. Schulze, E. GÜLZOW, St. Schönbauer, T. Knöri, R. Reissner, *J. Power Sources* 173 (2007) 19–27.
- [49] M.M. Mench, E.C. Kumbur, T.N. Veziroglu, *Polymer Electrolyte Fuel Cell Degradation*, Academic Press, 2011, p. 215.
- [50] S.J. Gregg, K.S.W. Sing, *Adsorption, Surface Area and Porosity*, Academic Press, 1982, p. 111.
- [51] J.H. Nam, M. Kaviani, *Int. J. Heat Mass Transf.* 46 (2003) 4595–4611.
- [52] A.Z. Weber, J. Newman, *J. Electrochem. Soc.* 152 (2005) A677–A688.
- [53] T.E. Springer, T.A. Zawodzinski, M.S. Wilson, S. Gottesfeld, *J. Electrochem. Soc.* 143 (1996) 587–599.